JOURNAL OF THERMOPHYSICS AND HEAT TRANSFER
Vol. 18, No. 4, October–December 2004

Three-Dimensional Distributed Mass Weighting for Noninverted Convective Skew Upwinding

E. O. B. Ogedengbe* and G. F. Naterer†
University of Manitoba, Winnipeg, Manitoba R3T 2N2, Canada

Numerical studies of skew upstream differencing are presented for three-dimensional convective heat transfer problems. Two new types of noninverted skew upwind schemes are developed and compared, so that local inversion of influence coefficient matrices is not required. Unlike previous schemes, skew upwind values of temperature are expressed explicitly in terms of surrounding nodal variables. Different mass weighting alternatives, including 3-node/3-point and 4-node/8-point formulations are developed and evaluated. Results are presented for three application problems, that is, convective step change of temperature, tank inflow/outflow, and radial heat flow in a rotating hollow sphere. Although the effects of upwind nodal asymmetry appear minor in the first and second problems, noticeable improvement with 4-node/8-point interpolation is observed in the rotating sphere problem. Additional reduction of CPU time due to noninverted convective upwinding is reported.

Nomenclature

C_{up}	=	convective length scale in upstream direction
c_p	=	specific heat, J/kgK
D	=	diffusion length scale
e^*	=	error at the center of the sphere
$\hat{\boldsymbol{i}}, \hat{\boldsymbol{j}}, \hat{\boldsymbol{k}}$	=	unit vectors in the x, y, and z directions
J	=	Jacobian determinant
k	=	thermal conductivity, W/mK
$\dot{M}$	=	combined mass flow rate, kg/s
$\dot{m}$	=	mass flow rate, kg/s
N_i	=	interpolation shape function at local node i
n	=	normal direction
Pe	=	Peclet number
Q	=	flow of ϕ
r_1, r_2	=	inner, outer radius of sphere, m
S	=	source term
$\hat{s}$	=	streamwise coordinate
T_1, T_2	=	inner, outer temperature of sphere, °C
t	=	time, s
u, v, w	=	fluid velocity components in the x, y, and z directions
v	=	fluid velocity vector, m/s
$\bar{v}$	=	average velocity magnitude, m/s
x, y, z	=	global Cartesian coordinates, m
Γ	=	diffusion coefficient
$\Delta n, \Delta l, \Delta m$	=	normal and tangential length scales
ρ	=	fluid density, kg/m^3
ϕ	=	scalar dependent variable
ω	=	angular velocity of sphere about the x axis, rad/s

Subscripts

c	=	convection
d	=	diffusion
i	=	local node number
ip	=	integration point
up	=	upwind

Superscripts

n	=	previous time level
$n+1$	=	current time level

Presented as Paper 2004-995 at the AIAA 42nd Aerospace Sciences Meeting and Exhibit, Reno, NV, 5–8 January 2004; received 2 February 2004; revision received 3 April 2004; accepted for publication 6 April 2004.

*Ph.D. Candidate, Department of Mechanical and Manufacturing Engineering, 15 Gillson Street. Member AIAA.

†Professor, Department of Mechanical and Manufacturing Engineering, 15 Gillson Street.

I. Introduction

SIMULATION time and accuracy are major factors that characterize the performance of predictive tools for numerical heat transfer. If the CPU run-time can be appreciably reduced without sacrificing accuracy, then a worthwhile contribution can be realized. Faster thermal simulations can give companies a competitive advantage in various ways. More cases of added complexity could be studied and optimized, thereby allowing the simulation tool to be more closely integrated into the design cycle. If a numerical simulation is too time consuming in an industrial setting, then it may not be fully accommodated within a tight product development schedule. Also, the time taken to bring the product to market may be lengthened, thereby adversely affecting the potential profit margins.

More specifically, convection modeling is a time-consuming portion of a numerical heat transfer simulation. In finite volume schemes, predictions are needed for the upwind value crossing the edge of the control volume. The upwind differencing scheme (UDS) uses the nodal value on the upstream side of the control volume, whereas a central differencing scheme (CDS) takes an average value between upstream and downstream nodes.[1] Because the weighting factor depends on the relative magnitudes of advection and diffusion, hybrid schemes such as the exponential differencing scheme (EDS) use the local Peclet number in this weighting.

It is well known that UDS leads to false diffusion errors when the flow direction is not closely aligned with the grid lines. Skew upstream differencing[2] and the conservative low-dispersion algorithm[3] (CLDA) have been shown to reduce such false diffusion errors by addressing the flow directionality. Carey et al.[4] have reduced false diffusion errors by interpolating values from upwind corner cells in the skew upwind corner convection algorithm (SUCCA). However, higher accuracy comes at the expense of about 20% additional CPU time during their simulations. This article attempts to include corner nodes in a 4-node/8-point scheme, while simultaneously reducing CPU run-time requirements.

Mass weighted differencing can be effectively applied to convective skew upwinding.[5] Muir and Baliga[6] show that flow-oriented interpolation with four-noded tetrahedral elements becomes sensitive to the local Peclet number and flow directionality. Despite its

benefits, directional upwind differencing may lead to other instabilities involving numerical dispersion.[7] Numerical dispersion has been reduced in convection modeling, but often at the expense of upstream values exceeding their physical bounds,[8] thereby producing nonphysical results.[3] Zhu and Rodi[9] develop a bounded upwind formulation that exhibits low dispersion.

It is essential that certain upwind variables, such as turbulence kinetic energy or species concentration, remain bounded within physical limiting values. Darwish and Moukalled[10] address modeling of skew upwind schemes, in view of ensuring such bounds. Gaskell and Lau[11] develop curvature-based corrections for convective upwinding, so that boundedness is preserved. Smith and Hutton[12] and Albada et al.[13] compare various computational methods, and report that nonlinear convective upwinding may produce nonphysical results when boundedness is not preserved.[3]

Conventional upwind schemes, such as UDS, exhibit first-order accuracy, and they may violate local entropy-stability criteria.[14] Second-order methods such as QUICK[15] use quadratic interpolation, involving values at three adjacent nodal points to reduce errors related to numerical diffusion. Agrawal[16] develops a third-order upwind scheme for viscous flows. However, a compromise is needed between higher-order accuracy and the resulting CPU run-time. For example, a lower-order scheme with more elements can often outperform a higher-order scheme for a given CPU run-time. Also, third-order accuracy may sacrifice boundedness in the convective upwinding.[3,17] Second-order accuracy with positive coefficients for numerical stability has been reported by Schneider and Raw.[18] However, if both nodal and integration point variables are used implicitly for convective upwinding, costly subelement inversion of the upwind coefficient matrices is needed.

Solution convergence represents another significant portion of simulation time. Hutchinson and Raithby[19] utilize a multigrid method, whereby coarse and fine grids are used together to accelerate solution convergence and reduce solution errors. Furthermore, entropy and the Second Law offer useful ways of establishing error indicators, either by an apparent entropy production difference,[20] or a weighted entropy residual.[21] Reduced error often leads to improved solution convergence and less simulation time. Such time and accuracy goals become particularly significant when predicting three-dimensional flows, such as turbomachinery flows[22] or multiphase flows.[23]

This paper develops two alternative skew upwind schemes for three-dimensional, incompressible flows. Advantages of 4-node/8-point interpolation with corresponding nodal mass weighting of upwind variables are examined. Performance of the new schemes is reported through applications to three test problems. These test problems involve a convective step change of temperature, combined advection and diffusion in a tank inflow/outflow problem, and radial heat flow in a rotating hollow sphere. Also, the CPU run-time savings of the new schemes are compared with an upwind procedure requiring inversion of the influence coefficient matrices. In this article, the new schemes will be called 3-node/3-point and 4-node/8-point noninverted skew upwind scheme (NISUS).

II. Numerical Formulation

The governing equation is expressed in the following divergence form,

$$\frac{\partial(\rho\phi)}{\partial t} + \nabla\cdot(\rho v\phi) + \nabla\cdot(\Gamma\nabla\phi) = S \tag{1}$$

In this equation, ϕ is a general scalar variable (such as energy per unit mass, turbulent kinetic energy, or concentration of a pollutant in an airstream), ρ is the mass density, v is the fluid velocity vector, Γ is the diffusion coefficient, and S is the volumetric generation rate. The conservation principle for ϕ may be applied to a finite control volume V, fixed in space and encompassed by a surface S. By application of Gauss's theorem to Eq. (1),

$$\int_V \frac{\partial(\rho\phi)}{\partial t}\mathrm{d}V + \int_S (\rho v\phi)\cdot \mathrm{d}\boldsymbol{n} + \int_S (\Gamma\nabla\phi)\cdot \mathrm{d}\boldsymbol{n} = \int_V S\,\mathrm{d}V \tag{2}$$

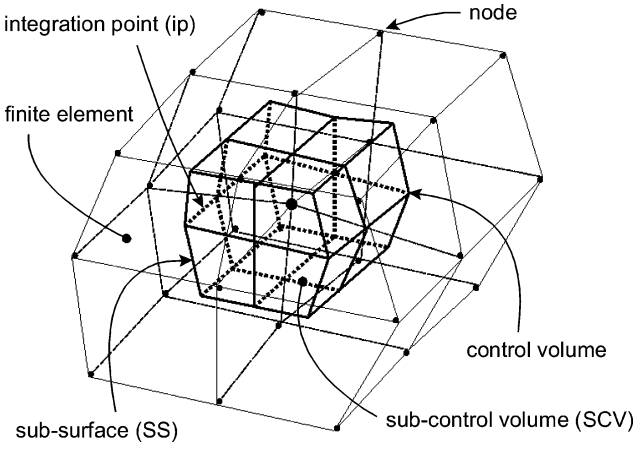

Fig. 1 Discretization of control volume and finite elements.

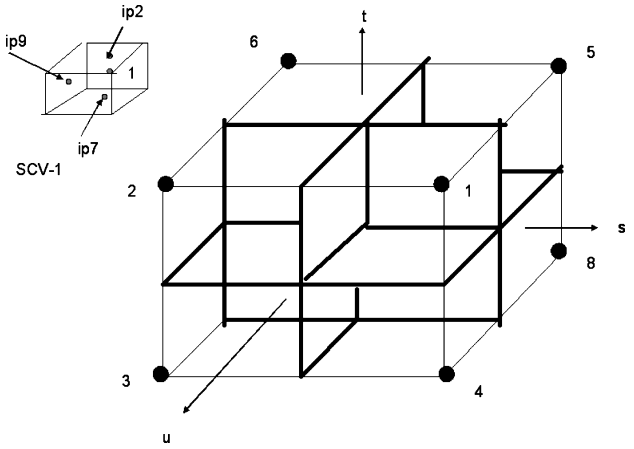

Fig. 2 Subdivision of finite element into eight subcontrol volumes.

where d$\boldsymbol{n}$ is the outward normal vector to the surface. In Eq. (2), the terms (left to right) refer to transient, convection, diffusion, and source/sink terms, respectively.

A control-volume-based finite element method (CVFEM) is used for the problem discretization. A typical three-dimensional control volume is shown in Fig. 1, including eight highlighted subcontrol volumes from eight surrounding hexahedral elements. Each element contains eight subcontrol volumes with a local coordinate system (s, t, u) (Fig. 2). Within an element, the dependent scalar variable is approximated by

$$\phi = \sum_{i=1}^{8} N_i \Phi_i \tag{3}$$

where Φ_i are the nodal values at local nodes, $i = 1, 2, \ldots, 8$. The shape function, N_i, is given by

$$N_i = \tfrac{1}{8}(1 + \tilde{s}s)(1 + \tilde{t}t)(1 + \tilde{u}u) \tag{4}$$

where

$$\tilde{s} = (+1, -1, -1, +1, +1, -1, -1, +1) \tag{5}$$

$$\tilde{t} = (+1, +1, -1, -1, +1, +1, -1, -1) \tag{6}$$

$$\tilde{u} = (+1, +1, +1, +1, -1, -1, -1, -1) \tag{7}$$

A complete control volume for a specific node is formed with eight subcontrol volumes from the eight surrounding finite elements joined to that node (Fig. 1, where the middle large dot is associated with the eight subcontrol volumes). Each finite element contributes three faces to the edges of the complete control volume. The surface

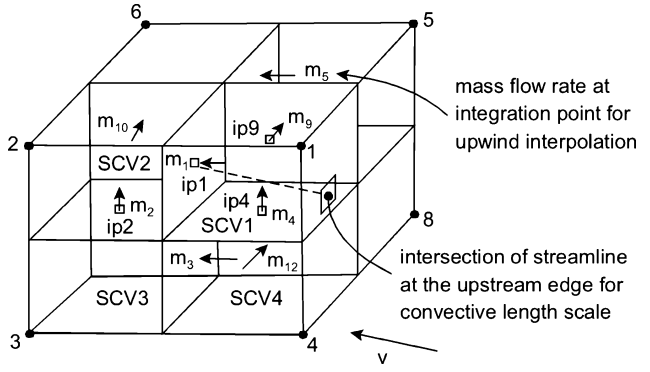

Fig. 3 Mass flow rates at each subsurface.

flux terms of Eq. (2) will be approximated by a dot product of each term with the normal vector at the surface midpoint (called the integration point).

The discrete equation for subcontrol volume (SCV) 1 becomes (Fig. 3)

$$Q_{\text{ip2}} + Q_{\text{ip7}} + Q_{\text{ip9}} + \int_{\text{SCV1}} S\,\mathrm{d}V = \frac{\partial}{\partial t}\int_{\text{SCV1}} \rho\phi\,\mathrm{d}V \tag{8}$$

where Q_{ip2}, Q_{ip7}, and Q_{ip9} refer to flows of ϕ across subsurfaces 2, 7, and 9, respectively, within the element. The flows of ϕ into/out of the subcontrol volume that are exterior to the element, as contributions from any of the adjacent elements or the domain boundary, are not included in Eq. (8). These flows do not require evaluation at a subelement level because their contributions are mutually self-canceled at the interior element surfaces through the assembly procedure, or the closure procedure at exterior element surfaces when boundary conditions are applied.

The three fluxes on the left side of Eq. (8) are the total fluxes across the subsurfaces bounding the first subcontrol volume (SCV1) in the element shown in Fig. 3. The flux across the subsurface (SS) at ip1 contains both diffusive and advective components, that is,

$$Q^{d,c}_{\text{ip1}} = \int_{\text{SS1}} -\boldsymbol{q}^d \cdot \mathrm{d}\boldsymbol{s} + \int_{\text{SS1}} -\boldsymbol{q}^c \cdot \mathrm{d}\boldsymbol{s} \tag{9}$$

where

$$\boldsymbol{q}^d = \nabla(\Gamma\phi) \tag{10}$$

$$\boldsymbol{q}^c = \rho v\phi \tag{11}$$

Then, the total flux for SCV1 becomes

$$Q^{d,c} = Q^{d,c}_{\text{ip1}} + Q^{d,c}_{\text{ip4}} + Q^{d,c}_{\text{ip9}} \tag{12}$$

Also, the transient term in Eq. (8) is approximated by

$$\frac{\partial}{\partial t}\int_{\text{SCV1}} \rho\phi\,\mathrm{d}V = \frac{\rho}{\Delta t}|\mathrm{Det}(J_1)|\left(\phi_1^{n+1} - \phi_1^n\right) \tag{13}$$

where the superscripts $n+1$ and n refer to current and previous time levels, respectively. Also, J_1 refers to the Jacobian of transformation between local and global coordinates. The remaining source term in Eq. (8) is integrated spatially over SCV1, based on its given (or known) spatial distribution.

Apart from the diffusive terms in Eqs. (9) and (10), which are evaluated by shape functions after differention of Eq. (3), the advective component in Eqs. (9–11) remains unknown. Past skew upwind schemes have often required local inversion of influence coefficient matrices, to express integration point variables solely in terms of nodal variables.[18] Such matrix inversions become costly, particularly as the number of nodal points increases. As a result, the following section considers two alternative noninverted methods, called 3-node/3-point and 4-node/8-point NISUS.

III. Convective Upwinding Procedure

When the convective term is evaluated at integration points in Eq. (2), past skew upwind schemes have expressed the integration point variables implicitly in terms of other integration point and nodal variables. These interrelationships lead to elemental influence coefficient matrices involving 12 integration points and eight nodal variables for an eight-noded hexahedral element. Matrix inversion is needed to represent the integration point variables explicitly in terms of nodal variables. Avoidance of such inversion, while ensuring that accuracy is maintained or improved, is a worthwhile objective, particularly for reduction of CPU run-time in three-dimensional simulations. This section develops and compares two alternative noninverted schemes, based on asymmetric (3-node/3-point) and symmetric (4-node/8-point) mass-weighted interpolation.

A. Asymmetric Mass Weighting (3-Node/3-Point)

Consider integration point ip1 in Fig. 3. The direction of the flow through this point is needed to establish the upstream side of the subcontrol face. Given the direction of flow indicated by the arrow in Fig. 3, four subcontrol volumes associated with nodes 1, 4, 5, and 8 are used for interpolation and upwinding. The following procedure uses a 3-node/3-point interpolation. The mass flows entering each subcontrol volume through the external faces at ip1 are expressed as

$$\dot{M}_1 = -\dot{m}_1 + \dot{m}_4 - \dot{m}_9 \tag{14}$$

$$\dot{M}_2 = \dot{m}_1 + \dot{m}_2 - \dot{m}_{10} \tag{15}$$

The sign of $\dot{m}_1$ establishes the upstream direction and edge. The following interpolation for the upwind value is adopted, depending on this sign,

$$\phi_{\text{up}} = (\lfloor\dot{m}_2\rfloor/\dot{M}_{\text{tot,in}})\Phi_3 + (\lfloor\dot{m}_{10}\rfloor/\dot{M}_{\text{tot,in}})\Phi_6 + (\lfloor-\dot{M}_2\rfloor/\dot{M}_{\text{tot,in}})\Phi_2$$

$$\dot{m}_1 > 0, \qquad \text{into SCV1} \tag{16}$$

$$\dot{M}_{\text{tot,in}} = \lfloor\dot{m}_2\rfloor + \lfloor\dot{m}_{10}\rfloor + \lfloor-\dot{M}_2\rfloor$$

or

$$\phi_{\text{up}} = (\lfloor\dot{m}_9\rfloor/\dot{M}_{\text{tot,out}})\Phi_5 + (\lfloor\dot{m}_4\rfloor/\dot{M}_{\text{tot,out}})\Phi_4 + (\lfloor\dot{M}_1\rfloor/\dot{M}_{\text{tot,out}})\Phi_1$$

$$\dot{m}_1 \le 0, \qquad \text{out of SCV1} \tag{17}$$

$$\dot{M}_{\text{tot,out}} = \lfloor\dot{m}_9\rfloor + \lfloor\dot{m}_4\rfloor + \lfloor\dot{M}_1\rfloor \tag{18}$$

The positive-definite operator, $\lfloor\ \rfloor$, is defined as

$$\lfloor x\rfloor = \begin{cases} x, & \text{if} \quad x \ge 0 \\ 0, & \text{if} \quad x < 0 \end{cases} \tag{19}$$

The upper-case notation of Φ refers to nodal variable, whereas lower-case ϕ refers to an interpolated value within the element. The procedure of mass-weighted interpolation is heuristic because it is unproven by a rigorous mathematical proof. It serves as a useful physically based principle that predicts subelement flow behavior according to SCV mass flow rates. Because of the spatial discretization and discrete grid spacing, the subgrid fluid motion is unknown, and the algorithm needs heuristic subelement interpolation. However, after the upwinded quantity is interpolated, the integration point convected variable will be determined from a rigorously derived approximation of the momentum transport equation at the integration point.

B. Symmetric Mass Weighting (4-Node/8-Point)

With eight points under consideration (including the integration point), a symmetric mass weighting uses a 4-node/8-point representation for upwind interpolation. By an increase of the nodal influence and symmetry of upwind coefficients, additional accuracy and stability of the convection modeling may be realized. In this case, the

effective mass flow weighting of each subcontrol volume from the associated node is evaluated, as follows,

$$\dot{M}_1 = \dot{m}_1 + \dot{m}_9 - \dot{m}_4 \tag{20}$$

$$\dot{M}_4 = \dot{m}_3 + \dot{m}_4 + \dot{m}_{12} \tag{21}$$

$$\dot{M}_5 = \dot{m}_5 - \dot{m}_9 - \dot{m}_8 \tag{22}$$

$$\dot{M}_8 = \dot{m}_7 + \dot{m}_8 - \dot{m}_{12} \tag{23}$$

whereas the total influence is

$$\dot{M}_{\text{tot}} = \lfloor \dot{M}_1 \rfloor + \lfloor \dot{M}_4 \rfloor + \lfloor \dot{M}_5 \rfloor + \lfloor \dot{M}_8 \rfloor \tag{24}$$

The upwind interpolation function ϕ_{up} becomes

$$\phi_{\text{up}} = (\lfloor \dot{M}_1 \rfloor / \dot{M}_{\text{tot}})\Phi_1 + (\lfloor \dot{M}_4 \rfloor / \dot{M}_{\text{tot}})\Phi_4 + (\lfloor \dot{M}_5 \rfloor / \dot{M}_{\text{tot}})\Phi_5 + (\lfloor \dot{M}_8 \rfloor / \dot{M}_{\text{tot}})\Phi_8 \tag{25}$$

where the positive-definite operator $\lfloor\ \rfloor$ was defined in Eq. (19).

Equations (16), (17), and (25), together with analogous results for other upwind points, give results for upwind variables explicitly in terms of nodal variables. Based on the coefficients premultiplying each nodal variable, the upwind variable can be expressed as follows,

$$\phi_{\text{up}} = \sum_{i=1}^{8} N_{\text{up},i}\Phi_i \tag{26}$$

where N_{up} and Φ_i are the upwind influence coefficient nodal values of the dependent scalar.

The upwind coefficients are less than unity, positive, and their sum, over $i = 1, 2, \ldots, 8$, is unity (as expected). Unlike the trilinear interpolation adopted for diffusion terms in Eqs. (3) and (10), $N_{\text{up},i}$ reflects a mass-weighted (nonlinear) interpolation. The upwind quantity is bounded between the nodal values. It is considered that the distributed mass weighting with 4-node/8-point interpolation can more accurately predict the convected quantities in recirculating flows.

The integration point variable in the convective term of Eq. (2) is influenced locally by both advective and diffusive processes. In the following subsection, the preceding upwind values will be incorporated into the integration point equation involving these local transport processes.

C. Assembly of Integration Point Variables

To express the integration point variable in terms of the nodal values, a transport equation involving advection and diffusion is approximated at the integration point, that is,

$$\rho\bar{v}\frac{\partial\phi}{\partial\hat{s}} - \Gamma\nabla^2\phi = 0 \tag{27}$$

where

$$\bar{v} = \sqrt{u^2 + v^2 + w^2} \tag{28}$$

and $\hat{s}$ is the streamline coordinate. The convective term in Eq. (27) is approximated as follows,

$$\rho\bar{v}\frac{\partial\phi}{\partial\hat{s}} \approx \rho\bar{v}\left(\frac{\phi_{\text{ip}} - \phi_{\text{up}}}{C_{\text{up}}}\right) \tag{29}$$

The convective length scale C_{up} represents the displacement of the upwind point from the integration point. It is evaluated based on upwind and integration points as follows,

$$C_{\text{up}} \approx \sqrt{(x_{\text{up}} - x_{\text{ip}})^2 + (y_{\text{up}} - y_{\text{ip}})^2 + (z_{\text{up}} - z_{\text{ip}})^2} \tag{30}$$

Also, the diffusive term is represented by

$$\Gamma\nabla^2\phi \approx \Gamma\left(\frac{\sum_{i=1}^{8} N_i\Phi_i - \phi_{\text{ip}}}{D^2}\right) \tag{31}$$

where the diffusive length scale D is expressed as

$$1/D^2 \approx 2/\Delta n^2 + 8/3\Delta l^2 + 8/3\Delta m^2 \tag{32}$$

where the normal (Δn) component and the tangential components (Δl, Δm) represent the three length scales at the integration point.

By substitution of Eqs. (29) and (31) into Eq. (27),

$$\rho\bar{v}\left(\frac{\phi_{\text{ip}} - \phi_{\text{up}}}{C_{\text{up}}}\right) - \Gamma\left(\frac{\sum_{i=1}^{8} N_i\Phi_i - \phi_{\text{ip}}}{D^2}\right) = 0 \tag{33}$$

By isolation of the integration point variable,

$$\phi_{\text{ip}} = \frac{\rho\bar{v}D^2\phi_{\text{up}} + \Gamma C_{\text{up}}\sum_{i=1}^{8} N_i\phi_i}{\rho\bar{v}D^2 + \Gamma C_{\text{up}}} \tag{34}$$

By substitution of Eq. (26) into the first term of the numerator, the integration point variable becomes

$$\phi_{\text{ip}} = \frac{\rho\bar{v}D^2\sum_{i=1}^{8} N_{\text{up},i}\Phi_i + \Gamma C_{\text{up}}\sum_{i=1}^{8} N_i\Phi_i}{\rho\bar{v}D^2 + \Gamma C_{\text{up}}} \tag{35}$$

It can be verified that this result yields the proper elliptic behavior in the diffusive limit ($\bar{v} \to 0$), as well as the full upwind influence in the advection limit ($\Gamma \to 0$).

The result in Eq. (35) gives an explicit representation of ϕ_{ip} in terms of the nodal variables. Therefore, local inversion of the full 12×12 integration point influence matrix is avoided. Without this local inversion, it is viewed that computational savings (reduced CPU run-time) can be realized for three-dimensional simulations. Previous schemes have used implicitly related nodal and integration points variables for various reasons, including higher accuracy for recirculating flows and more robust pressure/velocity coupling to overcome the pressure checkerboard problem.[1] In contrast, the proposed scheme captures the convection influences from the integration point without requiring local inversion of the coefficient matrices. In the following section, it will be shown that this approach matches or exceeds solution accuracy and reduces CPU run-time as compared with other conventional methods.

IV. Results and Discussion

In this section, numerical results from three test problems will be presented and discussed. The problems involve 1) a convective step change of temperature, 2) inflow/outflow from a tank, and 3) radial heat flow in a rotating hollow sphere. For each problem, the mesh spacing was selected to match grid configurations reported in previous studies.[1,6,12,18,24–26] In this way, accuracy and CPU run-time of the newly proposed formulations can be properly compared against other conventional upwind schemes.

A. Convective Step Change of Temperature

In this problem, the solution domain is discretized with dimensions of a unit cube. The three cases under consideration have been previously examined by Muir and Baliga.[6] These cases are illustrated in Figs. 4–6, with a uniform velocity field shown as coplanar with *abcd*. The boundary values of ϕ are assigned with reference to the plane *a–b–c–d*. In this problem, $\phi = 10$ on one side of the plane, whereas $\phi = 0$ on the other side of the plane and $\phi = 5$ at the nodal points where the plane intersects the boundaries. The transport of ϕ is considered to be pure convection, and so the diffusion coefficient is zero (value of 10^{-10} used numerically).

Past studies[1,2] have investigated the numerical difficulties of false diffusion associated with the discontuous step change. False diffusion errors occur with upstream differencing applied to convective flows, particularly when the local streamline is not closely aligned with the local grid lines. In that case, convective upwinding leads to artificial diffusive smearing of the transported quantity. To deal

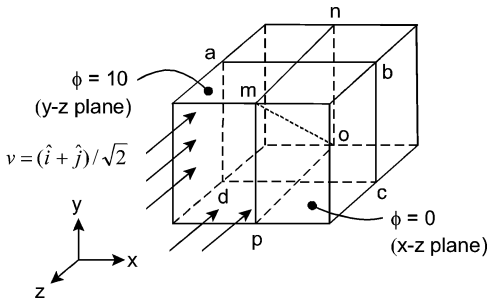

Fig. 4 Case 1: convective step change of temperature along *m–o*.

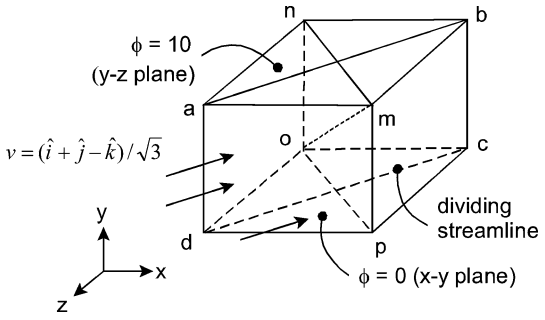

Fig. 5 Case 2: convective step change of temperature along *m–o*.

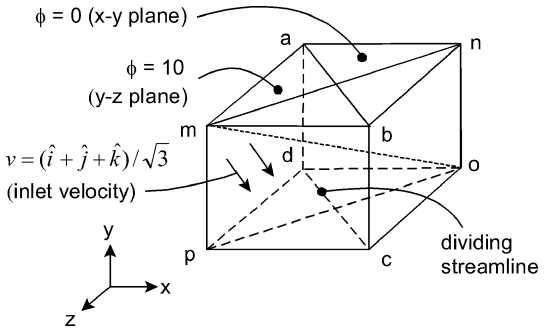

Fig. 6 Case 3: convective step change of temperature along *m–o*.

with such false diffusion errors, this article applies skew upwinding to the integration point equations for convective upwinding. Skew upwinding includes spatial effects of flow directionality on the upstream differencing, thereby reducing flase diffusion errors.[2]

The reduced form of the governing equation is

$$v \cdot \nabla \phi = 0 \tag{36}$$

and the velocity fields in the three cases are given by

$$\text{Case 1}: \quad v = \left(1/\sqrt{2}\right)(\hat{i} + \hat{j}) \tag{37}$$

$$\text{Case 2}: \quad v = \left(1/\sqrt{3}\right)(\hat{i} + \hat{j} - \hat{k}) \tag{38}$$

$$\text{Case 3}: \quad v = \left(1/\sqrt{3}\right)(\hat{i} + \hat{j} + \hat{k}) \tag{39}$$

In all of the cases, the converged results were obtained in less than 15 iterations. The predicted results of the scalar ϕ, along the diagonal *mo* on the plane *m–n–o–p* are presented for the three cases in Fig. 7. In view of maintaining mesh consistency when results are compared against previous studies, results from an $11 \times 11 \times 11$ mesh are shown in Fig. 7. Grids selected for other problems (Figs. 8–13) also reflect this consistency with past studies. For case 1 (Fig. 7a), all of the schemes (UDS, Muir/Baliga, 3-node/3-point NISUS and 4-node/8-point NISUS) perform well without false diffusion. This result is expected because the flow streamlines and the computational gridlines are aligned with each other. For cases 2–3 in

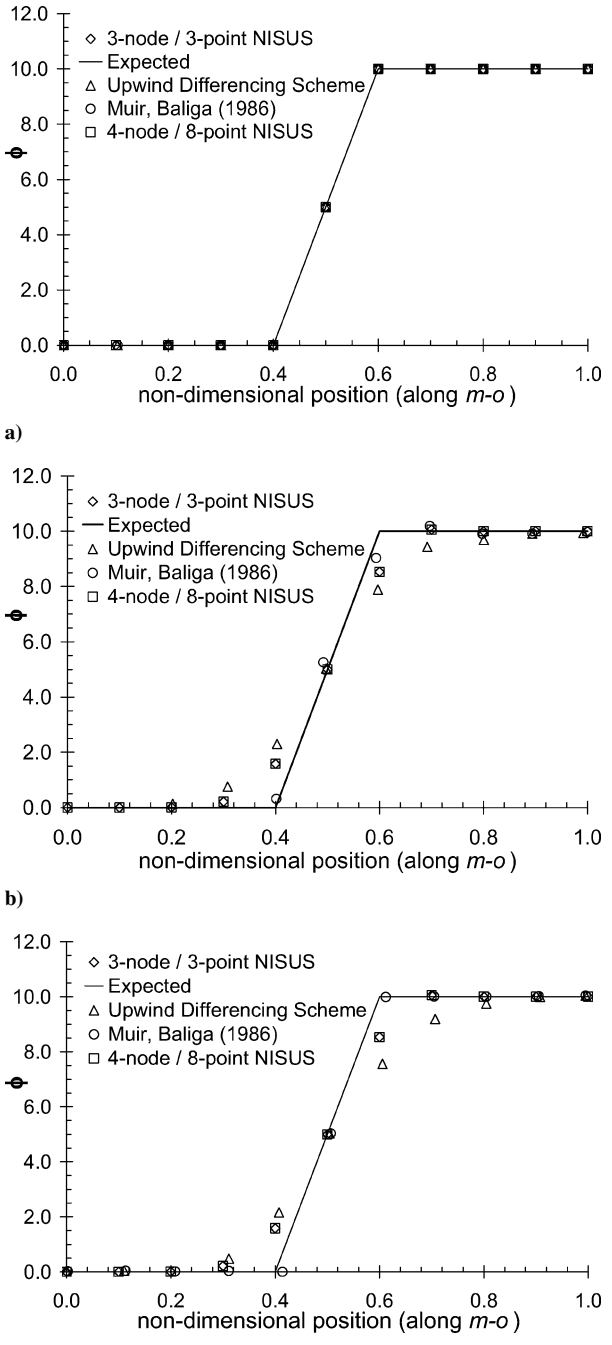

Fig. 7 Predicted results along *m–o*: a) case 1, $v_{in} = (\hat{i} + \hat{j})/\sqrt{2}$; b) case 2, $v_{in} = (\hat{i} + \hat{j} - \hat{k})/\sqrt{3}$; and c) case 3, $v_{in} = (\hat{i} + \hat{j} + \hat{k})/\sqrt{3}$.

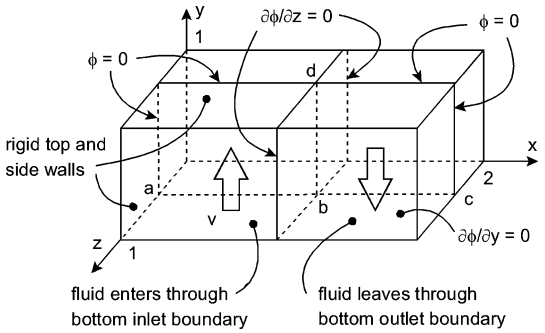

Fig. 8 Schematic of tank inflow/outflow problem.

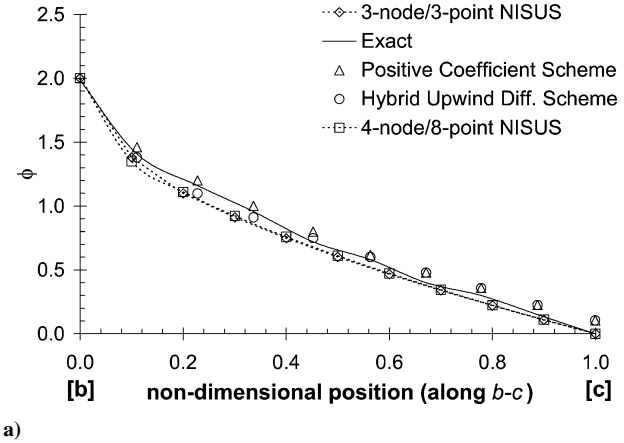

a)

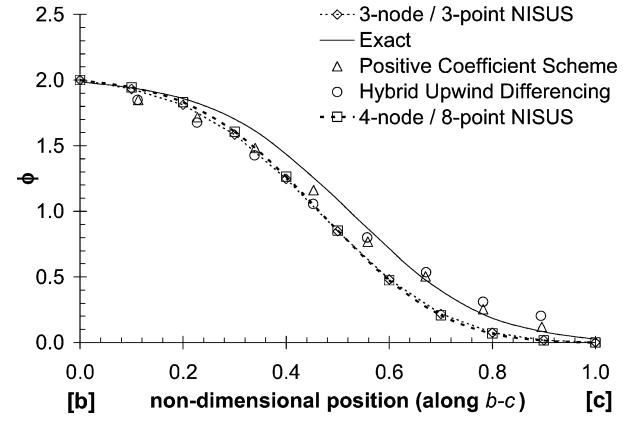

b)

Fig. 9 Predicted results along *b–c*: a) *Pe* = 10 and b) *Pe* = 100.

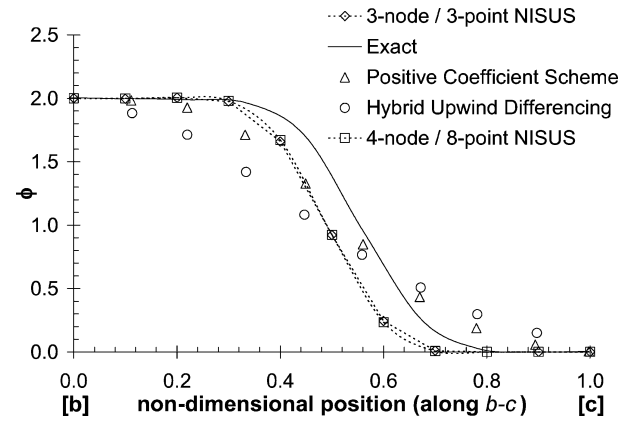

a)

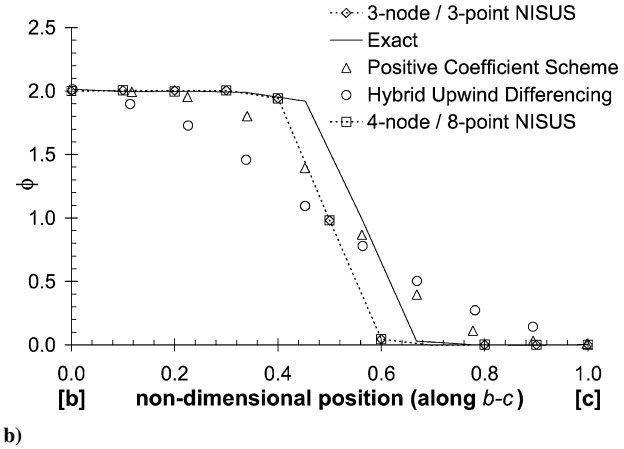

b)

Fig. 10 Predicted results along *b–c*: a) *Pe* = 500 and b) *Pe* = 10^6.

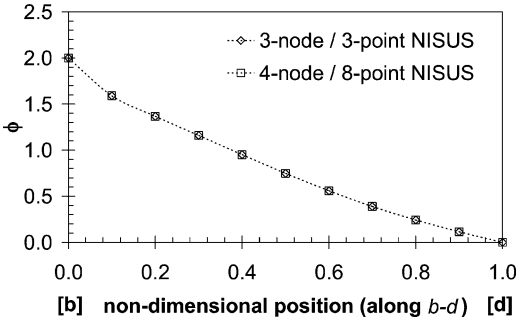

a)

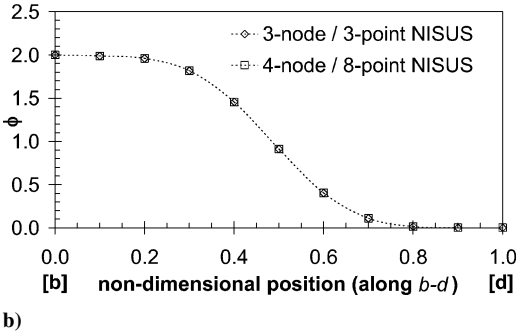

b)

Fig. 11 Predicted results along *b–d*: a) *Pe* = 10 and b) *Pe* = 100.

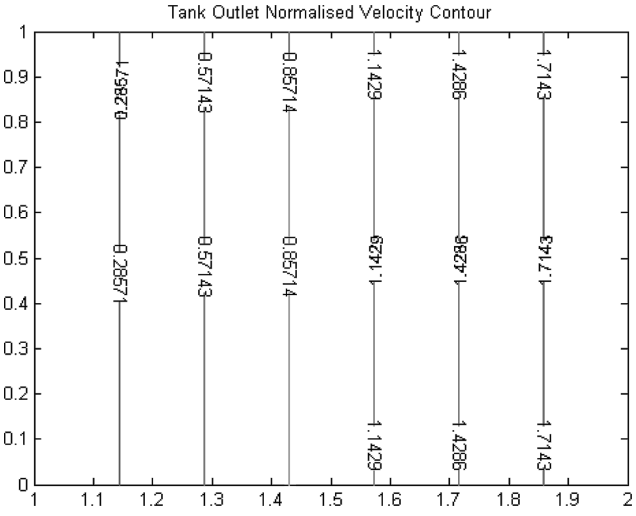

a)

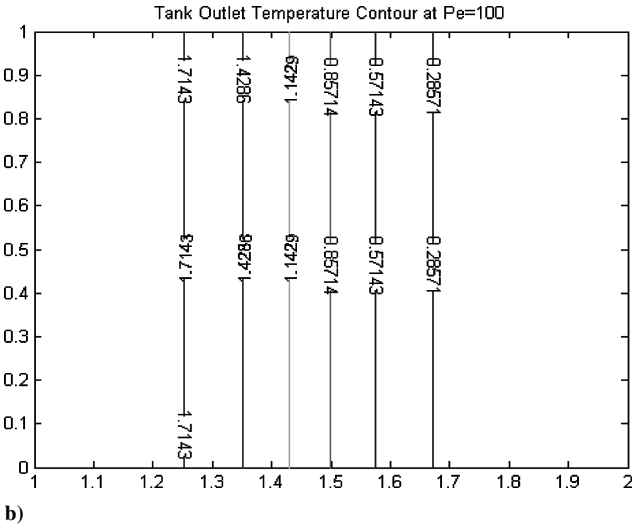

b)

Fig. 12 Predicted contours of a) velocity and b) temperature at *Pe* = 100.

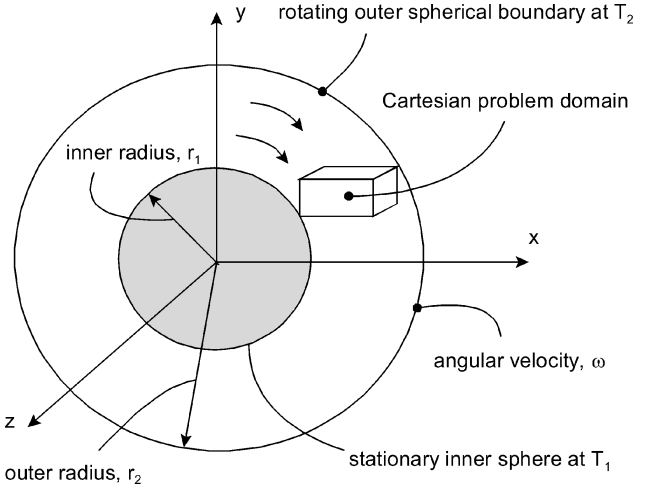

Fig. 13 Schematic of radial flow in a rotating hollow sphere.

Figs. 7b–7c, the results of Muir and Baliga[6] agree closely with the proposed scheme in terms of false diffusion, whereas they provide better accuracy than UDS. However, their results exhibit overshoots and undershoots for case 2, with slight variations in the levels of these oscillations. The 3-node/3-point and 4-node/8-point NISUS schemes exhibit similar performance and accuracy in each case. NISUS exhibits symmetry about the step-change location, without the overshoots and undershoots.

B. Tank Inflow/Outflow Problem

For this problem, results are presented for a solution domain discretized into $21 \times 11 \times 11$ nodes. This problem has been studied previously by various researchers for validation purposes.[12,18,24,25] The problem geometry and boundary conditions are shown in Fig. 8. The reduced form of the governing equation becomes

$$v \cdot \nabla\phi - (1/Pe)\nabla^2\phi = 0 \tag{40}$$

The analytical solution for the velocity field and the Peclet number are given by

$$v = 2y[1-(x-1)^2]\hat{\boldsymbol{i}} - 2(x-1)(1-y^2)\hat{\boldsymbol{j}} \tag{41}$$

$$Pe = \rho\bar{v}L/\Gamma \tag{42}$$

The boundary distribution of ϕ at the inlet is given by

$$\phi = 1 + \tanh[20(x-1)+10], \qquad 0 \le x \le 1 \tag{43}$$

The predicted results of temperature along b–c (outlet of the tank) according to four different schemes, with various Peclet numbers ranging from 10^1 to 10^6, are shown in Figs. 9 and 10. The four schemes are the hybrid upwind differencing scheme,[1,12] positive coefficient scheme,[18] 3-node/3-point NISUS and 4-node/8-point NISUS.

The accuracy of each scheme is assessed by the predicted profile of temperature and its spatial gradient along b–c at the outlet of the tank. By comparison of the results of various schemes with the exact solution, it can be observed that similar profiles are obtained at low Peclet numbers. The hybrid upwind differencing scheme exhibits a higher level of false diffusion when the Peclet number increases, whereas close agreement between both versions of NISUS is observed. However, the predicted temperature gradient at the outlet with NISUS exhibits close agreement with the exact solution and shows better agreement than results predicted by other schemes.

Also, the 3-node/3-point and 4-node/8-point NISUS are investigated through comparisons between the predicted profile of temperature along b–d. The predicted results at various Peclet numbers are shown in Fig. 11. The profile at the outlet of the tank is repeated along bd within the tank at various Peclet numbers. Close agreement between results of both schemes is observed. Evidence of grid convergence can be observed in Fig. 11 because the 3-node/3-point solutions agree closely with the 4-node/8-point results. Additional contour results of predicted velocity and temperature ($Pe = 100$) are shown in Fig. 12.

Although flow recirculation has occurred in this problem, the following problem entails stronger recirculation, where differences between versions of NISUS become more pronounced.

C. Radial Heat Flow in a Rotating Hollow Sphere

A schematic of this problem is shown in Fig. 13. Figure 13 depicts a hollow sphere with an inner radius r_1 and an outer radius r_2, which rotates with a constant angular velocity, $\hat{\omega} = \omega\hat{\boldsymbol{i}}$, about the x axis. The inner surface of the sphere is maintained at T_1 and the outer surface is kept at T_2.

This configuration has been studied previously by others.[6,26] The governing equation for the scalar variable (temperature) is

$$v \cdot \nabla\phi - (1/Pe)\nabla^2\phi = 0 \tag{44}$$

where the analytical solution of velocity and the Peclet number are given by

$$v = \omega y\hat{\boldsymbol{k}} - \omega z\hat{\boldsymbol{j}} \tag{45}$$

$$Pe = \rho c_p \omega r_1^2 \big/ k \tag{46}$$

The analytical solution of temperature is given by[6]

$$(T - T_2)/(T_1 - T_2) = 2\left[(x^2 + y^2 + z^2)\big/r_1^2\right] - 1 \tag{47}$$

A particular case of $r_2/r_1 = 2$ and $T_1 > T_2$ is considered. The results for this problem are evaluated in terms of the error e^* at the center point of the solution domain, that is,

$$e^* = \frac{|\phi(\text{analytical}) - \phi(\text{numerical})|}{\phi(\text{analytical})} \tag{46}$$

Sample predicted results of temperature and velocity contours at $Pe = 5000$ are shown in Figs. 14 and 15. In Fig. 16, numerical results are compared against various schemes, including the upwind differencing scheme, hybrid differencing scheme, power-law differencing scheme, flow-oriented interpolation scheme, 3-node/3-point NISUS and 4-node/8-point NISUS in the range of $0.01 \le Pe \le 10^4$. Larger numerical error is exhibited by the flow-oriented scheme of Muir and Baliga[6] at low Peclet numbers, whereas NISUS provides better accuracy than other schemes between $0.01 \le Pe \le 10^3$. Its numerical error is about 0.6%, when compared to the exact solution at Peclet numbers up to about 1000. The error falls to 0.3% at $Pe = 2250$, but rises up to 1.3% at $Pe = 5000$. The results show little or no difference in accuracy between the 3-node/3-point and 4-node/8-point NISUS at low Peclet numbers.

The flowfield within a rotating hollow sphere is considered to be more complex than the preceding problems, in terms of recirculation strength relative to diffusion, especially at higher Peclet numbers (beyond 10^3). Predicted results up to $Pe = 10^4$ indicate that better accuracy is achieved with NISUS, particularly with the 4-node/8-point NISUS. Additional NISUS points of interpolation become more significant for recirculating flows, when greater changes of flow directionality arise within a subelement.

At $Pe = 10^4$, the error remains below all of the past upwind schemes, except the results obtained previously by Muir and Baliga.[6] Past studies have shown that geometrical interpolation, domain discretization, and gridline alignment with respect to the flow direction can appreciably affect solution accuracy for three-dimensional flows.[26] For example, Muir and Baliga[6] have reported that tetrahedral elements can give more accurate results at higher Peclet numbers for flows in the rotating hollow sphere, as compared with hexahedral elements. Limitations of discretization of radial flow with hexahedral elements in NISUS become more pronounced at higher Peclet numbers. Predictions beyond $Pe = 10^4$ in Fig. 16 were not presented in the previous studies,[6,26] possibly due to factors such as turbulence or numerical instability. As a result, comparisons with

Table 1 Accuracy of numerical results for NISUS, UDS, and HDS

Problem	Exact (ideal)	NISUS	UDS	HDS	Muir and Baliga[6]
Convective step change, slope of ϕ at m–o midpoint, nondimensional 0.1 grid spacing					
1) $v_{in} = (\hat{i} + \hat{j})/\sqrt{2}$	50.0	50.0	50.0		50.0
2) $v_{in} = (\hat{i} + \hat{j} - \hat{k})/\sqrt{3}$	50.0	35.3	28.6		37.7
3) $v_{in} = (\hat{i} + \hat{j} + \hat{k})/\sqrt{3}$	50.0	35.3	25.3		49.6
Inflow/outflow tank, slope of ϕ at b–c midpoint, nondimensional 0.11 grid spacing					
1) $Pe = 10$	−1.26	−1.43	——	−1.32	——
2) $Pe = 100$	−3.64	−3.95	——	−2.36	——
3) $Pe = 500$	−6.63	−7.17	——	−2.83	——
4) $Pe = 1{,}000{,}000$	−7.57	−7.44	——	−2.80	——
Rotating hollow sphere, center-point percent error					
1) $Pe = 0.1$	0.0	0.58	1.20	1.20	1.20
2) $Pe = 1$	0.0	0.58	1.34	1.40	1.17
3) $Pe = 10$	0.0	0.58	3.07	1.35	1.56
4) $Pe = 100$	0.0	0.58	8.23	9.37	2.00
5) $Pe = 1{,}000$	0.0	0.56	9.66	9.74	2.76
6) $Pe = 10{,}000$	0.0	3.59	9.74	9.76	2.84

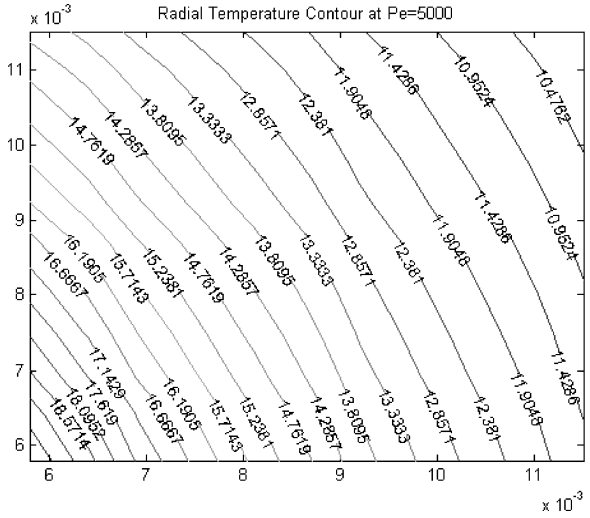

a) 3-node/3-point

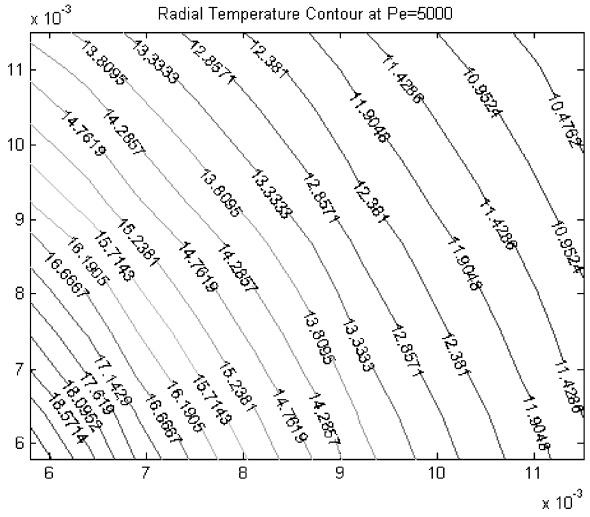

b) 4-node/8-point NISUS

Fig. 14 Temperature contours at $Pe = 5000$.

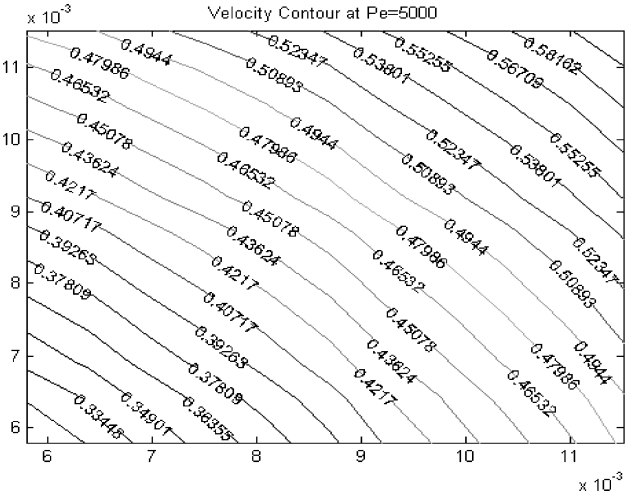

Fig. 15 Predicted velocity contours at $Pe = 5000$.

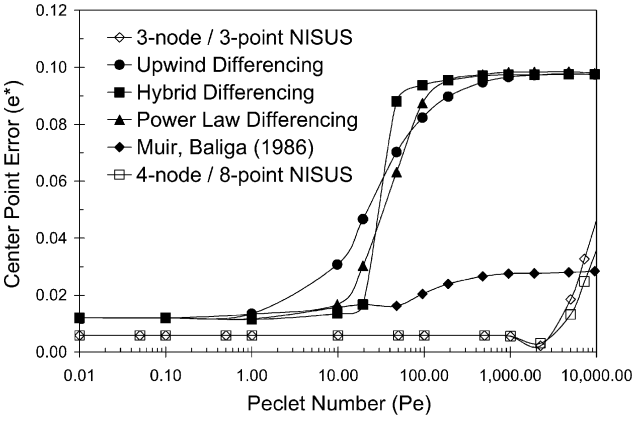

Fig. 16 Change of center-point error with varying Peclet numbers.

past schemes in Fig. 16 are shown only up to that point. Table 1 summarizes the numerical accuracy of predicted results for this problem, as well as results from the previous test problems.

The simulations were performed with a Pentium IV/2.60-GHz system and time step of 10,000 s (large time step for steady-state results). Solution convergence for different test cases was typically achieved within 15 iterations. The performance of the 3-node/3-point and 4-node/8-point NISUS, in terms of CPU run-time with different grid sizes has been investigated (Fig. 17). The two schemes (without local inversion) were compared with the same skew upwind procedure, but required local inversion of the upwind coefficient matrices.

Over the range of grid sizes considered, the CPU run-times for both noninverted schemes were nearly equal, with a CPU run-time of 6.4 s for the $11 \times 11 \times 11$ grid. However, an average CPU run-time of 8.0 s was observed when local inversion was used, thereby indicating a time-gain ratio of 1.25 for NISUS over the local inversion scheme. Thus, in addition to equal or better accuracy, the newly developed schemes exhibit appreciable savings of total CPU run-time when the number of nodal points increases. This advantage

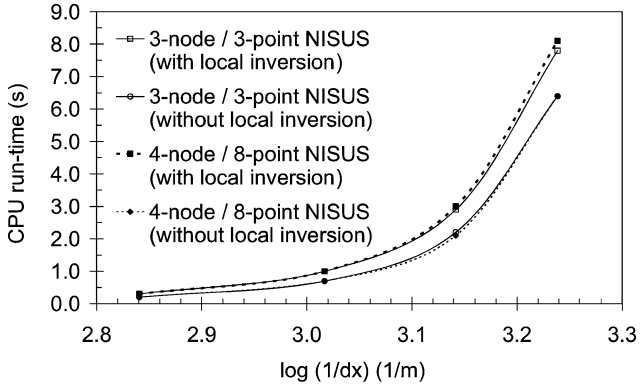

Fig. 17 Change of CPU time at varying grid spacings.

is viewed to have added significance for three-dimensional simulations because the number of grid points may rise substantially.

V. Conclusions

The performance of two NISUS methods is evaluated with respect to three test problems. The three problems are convective transport of a step change of temperature, advection/diffusion transport in an inlet/outlet tank, and radial heat flow in a rotating hollow sphere. The numerical results of both schemes reveal a similar level of accuracy and CPU run-time for the convective step change and advection–diffusion tank problems. However, a better level of accuracy was observed with the 4-node/8-point NISUS, as compared with the 3-node/3-point NISUS for radial heat flow in a rotating hollow sphere. The results indicate that the 4-node/8-point NISUS is better-suited for more complex recirculating flows. Symmetric mass weighting on upstream nodal values is achieved with that formulation, thereby allowing flow directionality of an additional nodal variable to be accommodated in the subelement interpolation. The results indicate that NISUS can outperform previous upwind schemes, in terms of both solution accuracy and CPU run-time. A CPU time-gain ratio of 1.25 was observed when local inversion of convection upwind variables is avoided.

Acknowledgments

Financial support from the Natural Sciences and Engineering Research Council of Canada as well as an E. R. Toporeck Graduate Fellowship in Engineering (E. O. B. Ogedengbe) are gratefully appreciated.

References

[1]Patankar, S., *Numerical Heat Transfer and Fluid Flow*, Hemisphere, Washington, DC, 1980.

[2]Raithby, G. D., "Skew Upstream Differencing Schemes for Problems Involving Fluid Flow," *Computer Methods in Applied Mechanics and Engineering*, Vol. 9, 1976, pp. 153–164.

[3]*PHOENICS Encyclopedia*, "Schemes for Convection Discretization," Simuserve, CHAM, Wimbledon Village, London, U.K., 1998.

[4]Carey, C., Scanlon, T. I., and Fraser, S. M., "SUCCA–A New Scheme to Reduce the Effects of Multidimensional False Diffusion," *PHOENICS Journal of CFD and Its Applications*, Vol. 5, No. 2, 1992, pp. 134–174.

[5]Hassan, Y. A., Rice, J. G., and Kim, J. H., "A Stable Mass-Flow-Weighted Two-Dimensional Skew Upwind Scheme," *Numerical Heat Transfer*, Vol. 6, 1983, pp. 395–408.

[6]Muir, B. L., and Baliga, B. R., "Solution of Three-Dimensional Convection—Diffusion Problems Using Tetrahedral Elements and Flow-Oriented Upwind Interpolation Functions," *Numerical Heat Transfer*, Vol. 9, 1986, pp. 143–162.

[7]Sharif, M. A. R., and Busnaina, A. A., "An Investigation into the Numerical Dispersion Problem of the Skew Upwind Finite Difference Scheme," *Applied Mathematical Modeling*, Vol. 12, 1988, pp. 98–108.

[8]Fromm, J. E., "A Method for Reducing Dispersion in Convective Difference Schemes," *Journal of Computational Physics*, Vol. 3, 1968, p. 176.

[9]Zhu, J., and Rodi, W., "A Low Dispersion and Bounded Convection Scheme," *Computer Methods in Applied Mechanics and Engineering*, Vol. 98, 1991, p. 345.

[10]Darwish, M., and Moukalled, F., "A New Approach for Building Bounded Skew-Upwind Schemes," *Computer Methods in Applied Mechanics and Engineering*, Vol. 129, No. 3, 1996, pp. 221–233.

[11]Gaskell, P. H., and Lau, A. K. C., "Curvature-Compensated Convective Transport: SMART, A New Boundedness-Preserving Transport Algorithm," *International Journal for Numerical Methods in Fluids*, Vol. 8, 1988, p. 617.

[12]Smith, R. M., and Hutton, A. G., "The Numerical Treatment of Advection: A Performance Comparison of Current Methods," *Numerical Heat Transfer*, Vol. 5, 1982, pp. 439–461.

[13]Van Albada, G. D., Van Leer, B., and Roberts, W. W., "A Comparative Study of Computational Methods in Cosmic Gas Dynamic," *Astronomy and Astrophysics*, Vol. 108, 1982, p. 76.

[14]Naterer, G. F., "Constructing an Entropy-Stable Upwind Scheme for Compressible Fluid Flow Computations," *AIAA Journal*, Vol. 37, No. 3, 1999, pp. 303–312.

[15]Leonard, B. P., "A Stable and Accurate Convective Modelling Proceudre Based on Quadratic Upstream Interpolation," *Computer Methods in Applied Mechanics and Engineering*, Vol. 19, 1979, pp. 59–98.

[16]Agrawal, R. K., "A Third-Order Accurate Upwind Scheme for Navier–Stokes at High Reynolds Numbers," *AIAA Journal*, Vol. 81, 1981, p. 112.

[17]Leonard, B. P., Leschziner, M. A., and McGuirk, J., "The QUICK Algorithm: A Uniformly 3rd-Order Finite-Difference Method for Highly Convective Flows," *Proceedings of the First Conference on Numerical Methods in Laminar and Turbulent Flow*, Swansea, 1978, p. 807.

[18]Schneider, G. E., and Raw, M. J., "A Skewed, Positive Influence Coefficient Upwinding Procedure for Control-Volume-Based Finite-Element Convection-Diffusion Computation," *Numerical Heat Transfer*, Vol. 9, 1986, pp. 1–26.

[19]Hutchinson, B. R., and Raithby, G. D., "A Multigrid Method Based on the Additive Correction Strategy," *Numerical Heat Transfer*, Vol. 9, 1986, pp. 511–537.

[20]Adeyinka, O. B., and Naterer, G. F., "Apparent Entropy Production Difference with Heat and Fluid Flow Irreversibilities," *Numerical Heat Transfer B*, Vol. 42, No. 5, 2002, pp. 411–436.

[21]Rinn, D., and Naterer, G. F., "Towards Entropy Detection of Anomalous Mass and Momentum Exchange in Incompressible Fluid Flow," *International Journal for Numerical Methods in Fluids*, Vol. 39, No. 11, 2002, pp. 1013–1036.

[22]Kictley, K. R., "Renormalization Group Based Algebraic Turbulence Model for Three Dimensional Turbomachinery Flows," *AIAA Journal*, Vol. 30, No. 6, 1992, pp. 1500–1506.

[23]Naterer, G. F., *Heat Transfer in Single and Multiphase Systems*, CRC Press, Boca Raton, FL, 2002.

[24]Schonauer, W., Raith, K., and Glotz, G., "The SLDGL Program Package for the Self-Adaptive Solution of Non-linear System of Elliptic and Parabolic PDEs," *Advances in Computer Methods/Partial Differential Equations*, Vol. 4, edited by R. Vichnevetsky and R. S. Stepleman, Rutgers Univ., New Brunswick, NJ, 1981, pp. 117–125.

[25]Schonauer, W., Raith, K., and Glotz, G., "The Self-Adaptive Solution of Non-linear 2-D Boundary Value Problems in Rectangular Domain," *Proceedings of the International Conference on Numerical Methods in Laminar and Turbulent Flow*, Venice, Italy, 1981.

[26]Prakash, C., "Examination of the Upwind Donor-Cell Formulation in Control Volume Finite-Element Methods for Fluid Flow and Heat Transfer," *Numerical Heat Transfer*, Vol. 11, 1987, pp. 401–416.